Structures of the Omicron Spike trimer with ACE2 and an anti-Omicron antibody

Wanchao Yin[1*], Youwei Xu[1*], Peiyu Xu[1*], Xiaodan Cao[2*], Canrong Wu[1*], Chunyin Gu[2*], Xinheng He[1,3], Xiaoxi Wang[1], Sijie Huang[1], Qingning Yuan[4], Kai Wu[4], Wen Hu[4], Zifu Huang[5], Jia Liu[2], Zongda Wang[2], Fangfang Jia[2], Kaiwen Xia[2], Peipei Liu[2], Xueping Wang[2], Bin Song[6], Jie Zheng[6], Hualiang Jiang[3,5,7], Xi Cheng[3,5], Yi Jiang[1,3,5], Su-Jun Deng[2], H. Eric Xu[1,3,7]

[1] The CAS Key Laboratory of Receptor Research, Shanghai Institute of Materia Medica, Chinese Academy of Sciences, Shanghai 201203, China

[2] Shanghai Jemincare Pharmaceuticals Co., Ltd., Shanghai, People's Republic of China

[3] University of Chinese Academy of Sciences, Beijing 100049, China

[4] The Shanghai Advanced Electron Microscope Center, Shanghai Institute of Materia Medica, Chinese Academy of Sciences, Shanghai 201203, China

[5] State Key Laboratory of Drug Research, Shanghai Institute of Materia Medica, Chinese Academy of Sciences, 555 Zu Chong Zhi Road, Shanghai 201203, China

[6] Immunological Disease Research Center, Shanghai Institute of Materia Medica, Chinese Academy of Sciences, 555 Zu Chong Zhi Road, Shanghai 201203, China

[7] School of Life Science and Technology, ShanghaiTech University, 201210 Shanghai, China

Correspondence should be addressed to Wanchao Yin (wcyin@simm.ac.cn) or Su-Jun Deng (dengsujun@jemincare.com) or H. Eric Xu (eric.xu@simm.ac.cn)

The Omicron variant (B.1.1.529) of SARS-CoV-2 has rapidly become the dominant infective strain and the focus efforts against the ongoing COVID-19 pandemic. Here we report an extensive set of structures of the Omicron spike trimer by its own or in complex with ACE2 and an anti-Omicron antibody. These structures reveal that most Omicron mutations are located on the surface of the spike protein, which confer stronger ACE2 binding but become inactive epitopes resistant to many therapeutic antibodies. Importantly, both RBD and the closed conformation of the Omicron spike trimer are thermodynamically unstable, with the melting temperature of the Omicron RBD decreased by as much as 7°C, making the spiker trimer prone to random open conformations. An unusual RBD-RBD interaction in the ACE2-spike complex unique to Omicron is observed to support the open conformation and ACE2 binding, serving the basis for the higher infectivity of Omicron. A broad-spectrum therapeutic antibody, which has completed Phase 1 clinical trial, is found to interact with the same two RBDs to inhibit ACE2 binding, in a mode that is distinguished from all previous antibodies, thus providing the structural basis for the potent inhibition of Omicron by this antibody. Together with biochemical data, our structures provide crucial insights into higher infectivity, antibody evasion and inhibition of Omicron.

The Omicron variant of SARS-CoV-2, the causative virus of COVID-19, was initially reported from South Africa on November 24 of 2021, and has become the dominant strain in less than a month, with daily infections close to one million cases worldwide and three quarters of which are infected with Omicron (*1*). Phylogenetic tree analyses reveal that Omicron is evolved independently from previous variants of concerns (VOC), including the predominant Alpha, Beta, Gamma, and Delta variants (Fig. 1A) *(2-5)*. Compared to the original wildtype (WT) strain of SARS-CoV-2, Omicron has an unusually high number of 60 mutations, over 50% of which (37 mutations) are located to the spike protein, the target of most COVID-19 vaccines and therapeutic antibodies (Fig. 1B) (*6-8*). This level of mutations has provided the genetic basis for Omicron to have the astounding ability in transmission, antibody evasion and vaccine resistance. However, the biochemical and structural mechanisms for Omicron's unusual capability remain unknown and require urgent studies given the astonishing rate of Omicron infections.

To study the biochemical mechanism for Omicron's enhanced transmission, we first biochemically characterized the interactions of the SARS-CoV-2 receptor ACE2 with the spike trimer from Omicron and the original WT strain. The monomeric human ACE2 bound to immobilized Omicron spike protein (K_D=2.07 nM) with approximately 9-fold higher affinity compared to that of WT spike protein (K_D=18.1 nM). The dimeric human ACE2 bound to immobilized biotinylated Omicron spike protein (K_D=0.485 nM) with approximately 8-fold higher affinity compared to that of WT (K_D=3.72 nM) (Fig. 1C). We then studied the interactions of ACE2 with isolated RBD from Omicron and WT strains. The monomeric human ACE2 bound to immobilized Omicron RBD (K_D=46.3 nM) with approximately 1.7-fold higher affinity compared to that of WT RBD (K_D=76.9 nM) (Fig. 1D). In biochemical investigation, enhanced interaction of Omicron spike and RBD proteins with human ACE2 was observed. These data were in agreement with previously published data (*9*), demonstrating the higher affinity of Omicron spike and RBD proteins to the SARS-CoV-2 receptor ACE2, thus conferring the increased infectivity of the Omicron variant.

To determine the structural basis of higher affinity of the Omicron spike protein to ACE2, we solved the structure of the ACE2-Omicron spike protein complex at a global resolution of 2.77 Å. Despite the excess amount of ACE2 (molar ratio of 3.2 ACE2 to 1 spike trimer), we only observed strong density for one ACE2 bound to one RBD from the spike trimer in the open “up” conformation (Fig. 2A, S1A and S1B, and S3), where the other two RBDs, with clear density, are in close “down” conformation. Surprisingly, particle classification revealed that the majority of picked particles (~70%) are absence of ACE2. The overall structure of the apo Omicron spike trimer reached a global resolution at 2.56 Å and resembles the structures of original WT strain (*10, 11*) and previous variants of concern (*12, 13*). In contrast to the clear visibility of the three RBDs in the ACE2-Omicron spike complex, the three RBDs in the apo Omicron spike trimer are nearly invisible in high resolution maps (Fig. S3A), and low resolution maps reveal that all RBDs are visible in down conformation (Fig. S3B), indicating that the RBD in the apo Omicron Spike complex is highly dynamic, preferentially in down state, whereas ACE2 binding helps stabilize the conformation of the three RBDs. Thermal shift assays revealed that both the Omicron and WT spike trimer displayed two melting temperatures with TM2 of 71.5 ° C identical for both spike trimers but with a TM1 difference by as much as 7.1 °C (Fig. S1C), which is nearly identical to the Tm difference between the isolated Omicron and WT RBDs (Fig. S1D), suggesting that the Omicron RBD is much less stable than the WT RBD in the spike trimer form or in isolated monomeric form (Fig. S2). The instability of the Omicron RBD probably synergizes with its higher binding affinity with ACE2 in promoting Omicron infectivity.

Mapping of the 37 mutations onto the up promoter of the ACE2 bound spike trimer reveals that most mutations are located on the surface of the spike protein, with many of them serving as the epitopes of therapeutic antibodies (Fig. 2B). Eight mutations in the NTD would affect the structures of the epitopes for a number of antibodies, for example, Δ143-145 would remove the epitope for 4A8 antibody (*14*).

15 mutations are in RBD, which contains the sites for ACE2 binding as well as the site for 90% of antibodies induced by infection or vaccination, are clustered into two hot spots (II and III), with 10 mutations in RBM and 5 mutations near the core structure domain (Fig. 2C). Both hot spots are the major epitopes for therapeutic antibodies LY-CoV 555, AZD1061, REGN10987. (*15-17*)

Local refinement of the ACE2-RBD region produced a high-quality map at 2.57 Å resolution, which allowed unambiguous building of the ACE2-RBD complex (Fig. 3A, Table S1). To our surprise, the overall structure of ACE2-RBDOmi complex is exceedingly similar to the two high resolution X-ray structures of the ACE2-RBDWT complex (PDB codes: 6LZG and 6M0J (18-19)), with the Cα atoms of the whole RBD deviated less than 0.4 Å (Fig. 3B, Table S2), despite the initial model used in our structure was from a cryo-EM structure (PDB code: 7A94) (*20*). Even more surprisingly, the backbone structure of the Omicron RBM is nearly identical to the WT RBM with RMSD of its Cα atoms less than 0.35 Å despite that there 10 mutations out of this 72 residues region. The extreme similarity of our ACE2-RBD^{Omi} complex structure to the two independent high resolution X-ray structures of the ACE2-RBD^{WT} complex reflects the high accuracy and quality of our cryo EM maps and structure modeling. The major differences residues in the ACE2-RBM interface, in which the Omicron RBM forms extra interactions with ACE2, including interactions from RRM mutations S477N, Q493R, Q496S, Q498R, and N501Y to ACE2 (Fig. 3C). In particular, the side chain of S477N forms two extra hydrogen bonds with S19 of ACE2; the Q498R mutation from two additional hydrogen bonds with Q42 and D38 from ACE2; and the N501Y mutation forms extensive packing interactions with ACE2 residues Y41 and K353. These additional interactions may compensate for the loss interactions caused by RBD mutations K417N, E484A and Y505H, which WT RBD residues forms polar interactions with ACE2 (Fig. 3C) (*21*).

Another surprising observation is an RBD-RBD interactions from one of the two down RBDs to the up RBD, with the interface comprised by residues A475, F486, and

Y489 from the down RBD and residues L368, Y369, F374, T385 and K386 from the up RBD (Fig. 3D, 3E). Structure comparison reveals that the RBD-RBD interface is not observed within the WT spike trimer because of a large movement of a loop (residues 368-374) as large as 7.4 Å, caused by Omicron RBD mutations S371L, S373P, G339D, and S375F, which also comprise a hotspot of epitopes (Fig. 3F, 3G, and Fig. 2C). This new RBD-RBD interaction may stabilize the up conformation of RBD that promotes ACE2 binding. Consistently, ACE2 binds to the Omicron spike trimer with 8-9 folds higher affinity than to the WT spiker trimer, but only 1.7 fold stronger to the RBD monomer (Fig. 1C,1D). Together, our biochemical data with these structural observations provide a mechanistic basis for the higher infectivity of the Omicron variant than the WT strain.

We had previously discovered an antibody, JMB2002, which showed potent efficacy against the WT SARS-CoV-2 in cell-based model as well as in rhesus monkey model (*22*). JMB2002 has finished Phase I clinical trial in healthy donors with excellent safety and PK properties and has been approved for clinical trial in US (IND 154745). To evaluate the neutralizing activity of JMB2002 against the Omicron variant, the binding affinity of JMB2002 to WT and Omicron spike proteins was determined. JMB2002 Fab recognized Omicron spike protein with 4-fold increased binding affinity (K_D=5.3 nM) compared to WT spike protein (K_D=20.4 nM). JMB2002 bound to the Omicron spike trimer with slightly higher affinity (K_D=0.47 nM) in comparison to that of WT (K_D=0.63 nM) (Fig. 4A-4D). Upon observation of higher affinity binding of JMB2002 to the Omicron spike protein, Omicron pseudo virus neutralization assay was performed to further confirm the neutralization ability of JMB2002. The results showed that JMB2002 could effectively block the entry of Omicron pseudo virus into human ACE2 expressing cells in addition to its blocking of the WT pseudovirus (Fig. 4E, 4F). JMB2002 was also able to neutralize a number of VOCs, including variants of Alpha, Beta, and Gamma, but not Delta (Fig. S4). Thus, JMB2002 may be an effective therapy against all WHO VOC except the Delta variant.

To reveal the basis of JMB2002 inhibition of Omicron, we solved the structure of the Omicron spike trimer bound to a Fab from JMB2002 at a global resolution of 2.80 Å (Fig. 5A, Table S1). To stabilize the constant regions of Fab, we used a nanobody that binds to the interface between the variable and constant regions of the heavy chain of Fab (*23*). The EM density maps reveal clear arrangement of the Fab-spike trimer complex, with the binding of 2 Fab molecules to the same two RBDs (one up and one down) from the ACE2-spike complex (Fig. 5A-5G). The overall structure of the spike trimer from the Fab-bound complex is very similar to that of the ACE2-bound complex, with an RMSD of 1.0 Å for the entire Cα atoms of the spiker trimer, including the RBD-RBD dimer configuration that is unique to Omicron (Fig. S6A, 6B).

Within the Fab-spike trimer structure, both Fab binds to the same region in the RBD (Fig. 5D). Within the isolated RBD, the Fab binding site does not overlap with the ACE2 binding site (Fig. S6C). However, within the spike trimer, Fab binding to the down RBD will clash with ACE2 binding to the up RBD (Fig. 5G), preventing the ACE2 binding in a conformation-specific state. Thus, the JMB2002 Fab inhibits ACE2 binding to the spike trimer through stabilizing a specific conformation that is clashed with ACE2 binding. Simultaneous binding of two Fab molecules to the spike trimer is consistent with 10-fold higher affinity of the IgG format of JMB2002 than the Fab format (Fig. 5A and Fig. 4F).

The L452R mutation in the Delta variant is at the center of the binding epitope of JMB2002 and this mutation will clash with Y102 from the heavy chain of Fab, thus providing an explanation for its loss of potency to the Delta variant (Fig. 5H, 5I). In addition, the binding site of the JMB2002 Fab to the RBD site in the spike trimer which is distinct from all previous class I to class IV antibodies (Fig. 5J), thus JMB2002 represents a new class of antibody to the spike trimer.

The astonishing spread of Omicron infections has taken the whole World to a great surprise, with extensive medical resources devoted to overcome this new wave of

pandemic (*24*). Mechanistic studies into the rapid pace of infection and immune evasion comprise of an integrated effort to combat Omicron infections. In this paper, we report three structures of the Omicron spike protein by its own or bound to the SARS-CoV-2 receptor ACE2 and a broad spectrum therapeutic antibody. Combined with the extensive biochemical and biophysical data, our results display that the extensive mutations in the Omicron spike proteins not only destabilize the closed conformation of the three RBD within the spike trimer but also increase the direct binding affinity by nearly 10 folds to its receptor ACE2, both of these properties serve as the basis for the higher infectivity of Omicron. The structure of the ACE2 bound Omicron spiker trimer reveal an unusual RBD-RBD interaction unique to Omicron and extra interactions in the ACE2-RBD interface, both of which contribute to the higher affinity of ACE2 to the Omicron spiker trimer, which could therefore lead to the higher infectivity of Omicron. Structural analyses of the Omicron spike trimer also reveals that its extensive mutations are mostly located on the hotspots of epitopes, providing a mechanistic basis for the outstanding capability of Omicron to escape most therapeutic antibodies and vaccinations.

In addition to revealing the mechanisms of increased infectivity and immune evasion, our antibody-bound Omicron spiker trimer also uncovers a distinguished mode of antibody binding to the spike trimer, in which the unique RBD-RBD configuration is preserved. The binding epitope of this broad spectrum antibody is different from all previous anti-SARS-CoV-2 antibodies, therefore opening a new venue for antibody drug discovery targeting various strains of SARS-CoV-2, including Omicron.

Figure Legends

Fig 1. SARS-CoV-2 Omicron spike protein with higher affinity to human ACE2 compared with SARS-CoV-2 wildtype. **(A)** Phylogeny of the SARS-CoV-2 variants. Variants of concern and variants of interest are labelled on the graph, the number of spike protein mutations are positively correlated with the distance from the original strain. The tree is constructed from the Nextstrain servers. **(B)** Schematic of Omicron spike protein domain architecture. The mutations of Omicron spike protein are labeled with different colors (blue for deleting mutation, red for inserting mutation). Mutations in RBM are compared with wildtype SARS-CoV-2 and four other variants of concern strains. SP, signal peptide; RBD, receptor binding domain; RBM, receptor binding motif; SD1, subdomain 1; SD2, subdomain 2; FP, fusion peptide; HR1, heptad repeat 1; HR2, heptad repeat 2; TM, transmembrane region; CT, cytoplasmic tail. **(C-D)** Binding of Omicron spike protein and wildtype SARS-CoV-2 spike protein to human ACE2 determined by BLI. KD values were determined with Octet Data Analysis HT 11.0 software using a 1:1 global fit model.

Fig 2. The structure of ACE2 Omicron spike trimer complex and epitopes of current antibodies. **(A)** Cryo-EM density of the ACE2-Omicron spike trimer complex. **(B)** The overall structure of the ACE2-Omicron spiker trimer complex and the locations of Omicron mutations. Epitope hotspots are highlighted in red circles with the number of antibodies indicated next to to the epitopes. **(C)** The histogram of epitope corresponding with residue number. Each epitope was counted if more than 3 heavy atoms of this residue are closer than 5 Å with the antibody. The structural component of SARS-CoV-2 is shown below.

Fig 3. Structural analysis of Omicron RBD and ACE2. **(A)** Cryo-EM density and location of Omicron RBD-ACE2 bound region. ACE2 is colored in orange. The Omicron ECD-trimer is colored in grey with two RBDs colored in purple and green. **(B)** ACE2-RBD binding interface. ACE2 is colored in orange and the RBD is colored in purple. Residues are shown in sticks with the correspondent cryo-EM density

represented in mesh. **(C)** Comparison of Omicron RBD-ACE2 and WT RBD-ACE2 interfaces. Left panel, an overall structural model of Omicron RBD-ACE2 bound region. Right-up panel, zoomed-in view of Omicron RBD-ACE2 with hydrogen bonds interactions. Right-down panel, the detailed hydrogen bonds interactions in WT RBD-ACE2 interfaces with the same view as in right-up panel. WT RBD is sea blue, Omicron RBD is purple, and ACE2 is orange. Hydrogen bonds interactions are in dotted lines. **(D)** The interaction interface between down RBD and ACE2-RBD. Left panel, overall cryo-EM density of down RBD-ACE2-RBD region. Right panel, a close-up view of RBD-RBD interaction. ACE2 bound RBD, also named up RBD here is in purple. The down RBD, which directly bounds to up RBD is in green. **(E)** The contribution of F486 and A475 from the down RBD in RBD-RBD interactions. F486 and A475 from down RBD in green, and F374, Y369, L368, T385, and K386 from up RBD in purple are shown in sticks. **(F)** Comparison of electrostatic potential maps between Omicron RBD (left panel) and WT RBD (right panel). Down RBD bound region in Omicron RBD and the correspondent region in WT RBD are highlighted in yellow boxes. Positive and negative charged regions are in blue and red, respectively. **(G)** The mutation-induced conformations change of Omicron RBD comparing with WT RBD.

Fig 4. Inhibition of ACE2 binding to the spike trimer by an anti-Omicron antibody. **(A)** Binding of JMB2002 Fab to Omicron and WT spiker trimer. **(B)** Binding of JMB2002 IgG to Omicron and WT spiker trimer. **(C)** Inhibition of the pseudo virus of WT and omicron by JMB2002.

Fig 5. Structure of Omicron S ECD antibody complex. **(A-C)** Cryo-EM density map of the Fab-bound Omicron S protein. The map showed with two front views **(A and B)** and a top view **(C). (D)** Superposition of the RBD-1 and RBD-2 both bound to a Fab molecule. **(E)** The interface between the up state RBD-1 and the down state RBD-2 of Omicron Spike protein. **(F)** The structure of the RBD-1 and RBD-2 bound to Fab. **(G)** Superposition of the ACE2-bound and Fab-bound RBD-1 shows the binding of

another Fab to RBD-2 inhibits ACE2 binds to RBD-1. **(H)** Omicron variant RBD L452 residue formed interactions with Fab. **(I)** The Delta variant L452R mutation clashes the Fab binding. **(J)** Binding modes of 4 representative 4 classes of antibody that neutralize SARS-CoV-2. PDB codes: class I, 7CM4; class II, 7CHF; class III, 7K90; class IV, 6WPS. The Fab in the Omicron S protein structure shows distinct binding modes from other 4 classes of antibodies.

Reference

1. J. Ai *et al.*, Omicron variant showed lower neutralizing sensitivity than other SARS-CoV-2 variants to immune sera elicited by vaccines after boost. *Emerg Microbes Infect*, 1-24 (2021).
2. M. Yuan *et al.*, Structural and functional ramifications of antigenic drift in recent SARS-CoV-2 variants. *Science* **373**, 818-823 (2021).
3. Y. Cai *et al.*, Structural basis for enhanced infectivity and immune evasion of SARS-CoV-2 variants. *Science* **373**, 642-648 (2021).
4. R. Earnest *et al.*, Comparative transmissibility of SARS-CoV-2 variants Delta and Alpha in New England, USA. *medRxiv*, (2021).
5. K. B. Pouwels *et al.*, Effect of Delta variant on viral burden and vaccine effectiveness against new SARS-CoV-2 infections in the UK. *Nat Med* **27**, 2127-2135 (2021).
6. L. Liu *et al.*, Striking antibody evasion manifested by the Omicron variant of SARS-CoV-2. *Nature*, preprint (2021).
7. D. Planas *et al*., Considerable escape of SARS-CoV-2 Omicron to antibody neutralization. *Nature*, preprint (2021).
8. Y. Cao *et al*., Omicron escapes the majority of existing SARS-CoV-2 neutralizing antibodies. *Nature*, preprint (2021).
9. M. McCallum *et al.*, Molecular basis of immune evasion by the Delta and Kappa SARS-CoV-2 variants. *Science* **374**, 1621-1626 (2021).
10. A. C. Walls *et al.*, Structure, Function, and Antigenicity of the SARS-CoV-2 Spike Glycoprotein. *Cell* **181**, 281-292 e286 (2020).
11. T. Zhou *et al.*, Cryo-EM Structures of SARS-CoV-2 Spike without and with ACE2 Reveal a pH-Dependent Switch to Mediate Endosomal Positioning of Receptor-Binding Domains. *Cell Host Microbe* **28**, 867-879 e865 (2020).
12. J. Zhang *et al.*, Structural impact on SARS-CoV-2 spike protein by D614G substitution. *Science* **372**, 525-530 (2021).
13. T. J. Yang *et al.*, Effect of SARS-CoV-2 B.1.1.7 mutations on spike protein structure and function. *Nat Struct Mol Biol* **28**, 731-739 (2021).
14. X. Chi *et al.*, A neutralizing human antibody binds to the N-terminal domain of the Spike protein of SARS-CoV-2. *Science* **369**, 650-655 (2020).
15. J. Hansen *et al.*, Studies in humanized mice and convalescent humans yield a SARS-CoV-2 antibody cocktail. *Science* **369**, 1010-1014 (2020).
16. B. E. Jones *et al.*, The neutralizing antibody, LY-CoV555, protects against SARS-CoV-2 infection in nonhuman primates. *Sci Transl Med* **13**, (2021).
17. D. Pinto *et al.*, Cross-neutralization of SARS-CoV-2 by a human monoclonal SARS-CoV antibody. *Nature* **583**, 290-295 (2020).
18. Q. Wang *et al.*, Structural and Functional Basis of SARS-CoV-2 Entry by Using Human ACE2 *Cell* **181**, 894-904 (2020).
19. J. Lan *et al.*, Structure of the SARS-CoV-2 spike receptor-binding domain bound to the ACE2 receptor. *Nature* **581**, 215-220 (2020).
20. D. J. Benton *et al.*, Receptor binding and priming of the spike protein of SARS-CoV-2 for membrane fusion. *Nature* **588**, 327-330 (2020).

21. Q. Wang *et al.*, Structural and Functional Basis of SARS-CoV-2 Entry by Using Human ACE2. *Cell* **181**, 894-904 e899 (2020).
22. C. Gu *et al.*, A human antibody of potent efficacy against SARS-CoV-2 in rhesus macaques showed strong blocking activity to B.1.351. *MAbs* **13**, 1930636 (2021).
23. Y. Yan *et al.*, Structure of an AMPK complex in an inactive, ATP-bound state. *Science* **373**, 413-419 (2021).
24. V. Thakur *et al*., OMICRON (B.1.1.529): A new SARS-CoV-2 Variant of Concern mounting worldwide fear. *J Med Virol*. preprint (2021).

Supplementary Information

Materials and Methods

Protein expression and purification

The N-terminal peptidase domain of human ACE2 (residues Ser19–Asp615) with an N-terminal GP67 signal peptide for secretion and a C-terminal 8×His tag for purification was inserted into a modified pFastBac vector (Invitrogen). All constructs were generated using the Phanta Max Super-Fidelity DNA Polymerase (Vazyme Biotech Co.,Ltd) and verified by DNA sequencing (Genewiz). Hi5 cell cultures were grown in ESF 921 serum-free medium (Expression Systems) to a density of 2-3 million cells per ml and then infected with baculoviruses for human ACE2 at a multiplicity of infection (m.o.i.) of about 5. The supernatant of cell culture containing the secreted peptidase domain of human ACE2 was collected 60h after infection, and then bound to Ni-NTA beads (Smart-Lifesciences). After wash with buffer without imidazole, the protein was eluted with buffer containing 300 mM imidazole, concentrated and then size-separated by a Superdex 200 Increase10/300 GL column in 25 mM HEPES pH 7.4, 150 mM sodium chloride. The fractions for the peptidase domain of human ACE2 were collected, concentrated to about 2 mg/ml, and stored at − 80 °C until use.

The SARS-CoV-2 Spike ECD and RBD proteins were all purchased from Sino Biological Inc., including Omicron spike ECD protein, Omicron spike RBD protein, WT spike ECD protein, WT spike RBD protein, Delta spike ECD protein, Delta spike RBD protein.

Nanobody (Nb) with a C-terminal His6 tag was expressed in the periplasm of *E.coli* strain BL21(DE3) bacteria (NEB). Cultures of 2L cells were grown to OD600 = 0.8 at 37°C, 180 r.p.m. in 2×YT media containing 100 μg/mL ampicillin. Then 0.1mM IPTG was added to the medium to induce protein expression at 28°C, 180 r.p.m. for another 8 h. Cells were harvested by centrifugation (5316g, 30 min) and disturbed in ice-cold buffer (20mM HEPES pH 7.4, 100mM NaCl), then centrifuged to remove cell

debris. Nb was purified by nickel affinity chromatography as previously described followed by size-exclusion chromatography using a HiLoad 16/600 Superdex 75 column. Selected fractions of Nb were finally concentrated to ~2 mg/ mL with 10% glycerol and kept frozen at -80°C for further use. The quality of purified proteins was assessed by SDS-PAGE.

Protein complex formation

For the ACE2 bound Omicron spike ECD protein complex, the Omicron spike ECD protein was incubated with purified peptidase domain of human ACE2 at molar ratios of 1:3.2 (spike trimer to peptidase domain of human ACE2) for 60 min on ice prior to purification by gel filtration chromatography using a Superose6 column (GE Healthcare) pre-equilibrated with TBS buffer (20mM Tris, pH8.0, 150mM NaCl). For the JMB2002Fab bound Omicron spike ECD protein complex, the Omicron spike ECD protein was incubated with JMB2002Fab d anti-Fab nanobody at molar ratios of 1:4:5 (spike trimer to JMB2002Fab to anti-Fab nanobody) for 60 min on ice prior to purification by gel filtration chromatography using a Superose6 column (GE Healthcare) pre-equilibrated with HBS buffer (25mM Tris, pH7.5, 150mM NaCl). For the Omicron spike ECD trimer protein only, the Omicron spike ECD protein was directedly set to purification by gel filtration chromatography using a Superose6 column (GE Healthcare) pre-equilibrated with TBS buffer (20mM Tris, pH8.0, 150mM NaCl) or HBS buffer (25mM Tris, pH7.5, 150mM NaCl). Fractions containing the complex were pooled and concentrated to 1.5-3 mg/ml.

Cryo-EM sample preparation and data acquisition

For the Omicron spike ECD trimer protein only at pH8.0, 3 μL of the Omicron spike ECD purified with TBS buffer at the concentration of 1.9 mg/ml were applied to glow-discharged UltrAuFoil Holey Gold 300 mesh grids (Au, R0.6/1); For the Omicron spike ECD trimer protein only at pH4.0, the Omicron spike ECD purified with HBS buffer at the concentration of 1.8 mg/ml was mixed with 1 M sodium acetate, pH4.0 (final sodium acetate concentration: 0.1 M), then 3 μL sample were applied to glow-

discharged UltrAuFoil Holey Gold 300 mesh grids (Au, R0.6/1); For the ACE2 bound Omicron spike ECD protein complex, 3 μL sample purified with TBS buffer at the concentration of 2.5 mg/ml were applied to glow-discharged UltrAuFoil Holey Gold 300 mesh grids (Au, R1.2/1.3); For the JMB2002Fab bound Omicron spike ECD protein complex, 3 μL sample purified with HBS buffer at the concentration of 2.5 mg/ml were applied to glow-discharged 300 mesh amorphous NiTi foil (Au, 1.2/1.3). Extra samples were blotted with filter paper for 3.0 s and plunge-frozen in liquid ethane using a FEI Vitrobot Mark IV. Cryo-EM micrographs were collected on a 300kV Titan Krios microscope (FEI) equipped with a K3 direct detection camera. For ECD-ACE2 dataset, 8,194 movies were collected, and for ECD-Fab dataset, 14,740 movies were collected on a Titan Krios equipped with a Gatan K3 direct electron detection device at 300kV with a magnification of 105,000, corresponding to a pixel size 0.824 Å. Image acquisition was performed with EPU Software (FEI Eindhoven, Netherlands). We collected a total of 36 frames accumulating to a total dose of 50 e^{-} $Å^{-2}$ over 2.5 s exposure.

Cryo-EM data processing

For ECD-ACE2 dataset, MotionCor2 was used to perform the frame-based motion-correction algorithm to generate drift-corrected micrograph for further processing and CTFFIND4 provided the estimation of the contrast transfer function (CTF) parameters[1,2]. 1,566 aligned micrographs were deleted because of contaminations or bad ice quality. After selection, approximately 1,500 particles were manually picked and two-dimensional (2D) classes were calculated and used as references for automatic picking. A total of 5,071,668 particles were extracted from the cryo-EM micrographs performed with Relion3.0[3]. All subsequent steps including 2D classification, three-dimensional (3D) classification, 3D refinement, and local refinement were performed using cryoSPARC[4], unless stated otherwise. Two rounds of reference-free 2D classification, yielding 854,875 particles after clearance. Three rounds hetero refinement separated out 522,186 particles that resulted to a clearer density of ECD-trimer structure at 2.56 Å global resolution. Two rounds hetero

refinement separated out 242,374 particles that resulted to a clearer density of ACE2 bound ECD-trimer structure at 2.77 Å global resolution. Local refinement focused on the ACE2-RBD or RBD-ACE2-RBD with masks could reconstitute ACE2-RBD and RBD-ACE2-RBD structures at 2.79 Å and 2.57 Å global resolution, respectively. Local resolution estimate was performed with cryoSPARC.

For ECD-Fab dataset, MotionCor2 was used to perform the frame-based motion-correction algorithm to generate drift-corrected micrograph for further processing and CTFFIND4 provided the estimation of the contrast transfer function (CTF) parameters[1,2]. Automated particle selection yielded 6,563,376 particles. Two rounds of reference-free 2D classification, yielding 5,022,550 particles after clearance. Three rounds hetero refinement separated out 421,216 particles that resulted to a clearer density of ECD-trimer structure at 2.76 Å global resolution. Fucus classification and local refinement focused on the RBD-Fab with masks could reconstitute a structure at 3.45 Å resolution. Local resolution estimate was performed with cryoSPARC.

Model building

ECD structure from Swiss-model prediction was used as the starting reference model for ECD-trimer building[5]. Structure of ACE2 derived from PDB entry 7KMB[6] was rigid body fit into the density. For the Fab-ECD complex, the structure of the SARS-CoV-2 spike glycoprotein (PDB: 6VXX[7]) and the Fab-nanobody-AMPK structure (PDB:7JHH[8]) were used as initial model. All models were fitted into the EM density map using UCSF Chimera[9] followed by iterative rounds of manual adjustment and automated rebuilding in COOT[10] and PHENIX[11], respectively. The model was finalized by rebuilding in ISOLDE[12] followed by refinement in PHENIX with torsion-angle restraints to the input model. The final model statistics were validated using Comprehensive validation (cryo-EM) in PHENIX[11]. All structural figures were prepared using Chimera[9], Chimera X[13], and PyMOL (Schrödinger, LLC.).

Measurement of human ACE2 binding to Omicron and WT spike RBD/ECD by biolayer interferometry

The binding of human ACE2 to Omicron and WT spike RBD/ECD were performed using Octet Red96e (Sartorius). The biotinylation of SARS-CoV-2 spike RBD or monomeric human ACE2 protein were carried out by using EZ-Link Sulfo-NHS-LC-Biotin kit (ThermoFisher Scientific, A39257) following the manufacturer's instruction. SA biosensors (Sartorius, 18-5020) were used to immobilize the biotinylated WT spike RBD protein (Sino Biological, 40589-V08H), Omicron SARS-CoV-2 spike RBD protein (Sino Biological, 40952-V08H121) or monomeric human ACE2 protein. The association of SARS-CoV-2 spike RBD-coated sensors with different concentrations of monomeric human ACE2 were recorded for 3 min prior to 10 min dissociation in kinetics buffer (0.02% Tween-20 in PBS). The binding of biotinylated monomeric human ACE2 to WT SARS-CoV-2 spike ECD (Sino Biological, 40589-V08B1) or Omicron SARS-CoV-2 spike ECD (Sino Biological, 40589-V08H26) was also evaluated. Protein A biosensors (Sartorius, 18-5012) were used to capture the dimeric human ACE2 (Sino Biological, 10108-H02H) followed by measuring the association and dissociation with WT or Omicron spike ECD protein. KD values were calculated with Octet Data Analysis HT 12.0 software using a 1:1 global fit model. Data were plotted using Prism V8.0 software (GraphPad).

Measurement of anti-SARS-CoV-2 antibody JMB2002 binding to Omicron and WT spike ECD by biolayer interferometry

The interaction of anti-SARS-CoV-2 antibody JMB2002 with Omicron and WT spike ECD was determined using Octet Red96e (Sartorius). SA biosensors (Sartorius, 18-

5020) were used to capture the biotinylated WT SARS-CoV-2 spike ECD protein (ACRO, SPN-C82E9) or Omicron SARS-CoV-2 spike ECD protein (ACRO, SPN-C82Ee). The association of SARS-CoV-2 spike protein-coated sensors with different concentrations of anti-SARS-CoV-2 antibody JMB2002 were recorded for 3 min prior to 10 min dissociation in kinetics buffer (0.02% Tween-20 in PBS). KD values were calculated with Octet Data Analysis HT 12.0 software using a 1:1 global fit model. Data were plotted using Prism V8.0 software (GraphPad).

Pseudovirus neutralization assay

In the pseudovirus neutralization assay, serial dilutions of JMB2002 IgG were preincubated with an equal volume of WT, Alpha, Beta, Gamma, Delta and Omicron pseudovirus (2×10^4 $TCID_{50}$/mL) for 1 h at 37°C. Subsequently, HEK293 cells stably expressing hACE2 (Vazyme, DD1401) (2×10^4 cells/well) were seeded in 96-well plates, treated with the corresponding pseudovirus and antibody mixtures, and incubated at 37°C for 48 h. Luciferase activity was measured using Bio-Lite Luciferase Assay System (Vazyme, DD1201). The neutralization inhibition rate was calculated with the following formula.

$$\text{Inhibition rate (\%)} = \left(1 - \frac{\text{mean intensity of sample} - \text{mean intensity of blank control}}{\text{mean intensity of negative control} - \text{mean intensity of blank control}}\right) X\, 100\%$$

IC_{50} values were calculated by a four-parameter logistic curve fitting approach in Prism V8.0 software (GraphPad).

Supplementary References

1 Zheng, S. Q. *et al.* MotionCor2: anisotropic correction of beam-induced motion for improved cryo-electron microscopy. *Nat Methods* **14**, 331-332, doi:10.1038/nmeth.4193 (2017).

2 Rohou, A. & Grigorieff, N. CTFFIND4: Fast and accurate defocus estimation from electron micrographs. *J Struct Biol* **192**, 216-221, doi:10.1016/j.jsb.2015.08.008 (2015).

3 Zivanov, J. *et al.* New tools for automated high-resolution cryo-EM structure determination in RELION-3. *Elife* **7**, doi:10.7554/eLife.42166 (2018).

4 Punjani, A., Rubinstein, J. L., Fleet, D. J. & Brubaker, M. A. cryoSPARC: algorithms for rapid unsupervised cryo-EM structure determination. *Nat Methods* **14**, 290-296, doi:10.1038/nmeth.4169 (2017).

5 Schwede, T., Kopp, J., Guex, N. & Peitsch, M. C. SWISS-MODEL: An automated protein homology-modeling server. *Nucleic Acids Res* **31**, 3381-3385, doi:10.1093/nar/gkg520 (2003).

6 Zhou, T. *et al.* Cryo-EM Structures of SARS-CoV-2 Spike without and with ACE2 Reveal a pH-Dependent Switch to Mediate Endosomal Positioning of Receptor-Binding Domains. *Cell Host Microbe* **28**, 867-879 e865, doi:10.1016/j.chom.2020.11.004 (2020).

7 Walls, A. C. *et al.* Structure, Function, and Antigenicity of the SARS-CoV-2 Spike Glycoprotein. *Cell* **181**, 281-292 e286, doi:10.1016/j.cell.2020.02.058 (2020).

8 Yan, Y. *et al.* Structure of an AMPK complex in an inactive, ATP-bound state. *Science* **373**, 413-419, doi:10.1126/science.abe7565 (2021).

9 Pettersen, E. F. *et al.* UCSF Chimera--a visualization system for exploratory research and analysis. *J Comput Chem* **25**, 1605-1612, doi:10.1002/jcc.20084 (2004).

10 Emsley, P. & Cowtan, K. Coot: model-building tools for molecular graphics. *Acta Crystallogr D Biol Crystallogr* **60**, 2126-2132, doi:10.1107/S0907444904019158 (2004).

11 Adams, P. D. *et al.* Recent developments in the PHENIX software for automated crystallographic structure determination. *J Synchrotron Radiat* **11**, 53-55, doi:10.1107/s0909049503024130 (2004).

12 Croll, T. I. ISOLDE: a physically realistic environment for model building into low-resolution electron-density maps. *Acta Crystallogr D Struct Biol* **74**, 519-530, doi:10.1107/S2059798318002425 (2018).

13 Pettersen, E. F. *et al.* UCSF ChimeraX: Structure visualization for researchers, educators, and developers. *Protein Sci* **30**, 70-82, doi:10.1002/pro.3943 (2021).

Fig. S1. Purification and characterization of the Omicron spike protein complex. (**A**) Gel filtration profile of the Omicron ECD-ACE2 complex, showing a sharp peak, and the SDS gel of the Omicron ECD-ACE2 complex, showing balanced ratios for each subunit. (**B**) Gel filtration profile of the Omicron ECD-Fab complex, showing a sharp peak, and the SDS gel of the Omicron ECD-Fab complex, showing balanced ratios for each subunit. (**C**) Thermal stability shift analysis of the Omicron and WT spike trimer. (**D**) Thermal stability shift analysis of the Omicron and WT RBD.

Fig. S2. Cryo-EM data processing of the Omicron ECD-ACE2 complex. (**A**) A representative cryo-EM micrograph of Omicron ECD-ACE2 complex with 50 nm scale bar included as a size reference. (**B**) Computational processing of cryo-EM data. (**C**) Twenty representative reference-free two-dimensional (2D) cryo-EM class averages reveal the ACE2 density (yellow arrow). (**D**) Local resolution of sub-reconstructions of RBD-ACE2 (left panel) and RBD-ACE2-RBD (right panel). Resolution bar is shown in the middle. (**E**) The FSC curves for the reconstructions. Color scheme: ECD-ACE2, black; RBD-ACE2, red; ECD-trimer, yellow; RBD-ACE2-RBD, blue. The resolution of the reconstructions using the Fourier shell cutoff at 0.143 is shown.

Fig. S3. Cryo-EM analysis of Omicron ECD-trimer. (**A**) High resolution density map of Omicron ECD-trimer after sharpening. Front and top views are shown. The densities for three RBDs are smeared. (**B**) Density map of Omicron ECD-trimer at low resolution without sharpening. The blob densities according to RBDs are shown in all-down conformation. Front and top views are shown. Three ECDs are colored in purple, green, and salmon.

Fig. S4 Neutralization of WT, Alpha, Beta, Gamma, and Delta pseudo-virus by JMB2002. Delta IC50 values were calculated by Prism V8.0 software using a four-parameter logistic curve fitting approach.

Fig. S5. Cryo-EM data processing of the Omicron ECD-Fab complex. (**A**) Flow chart of cryo-EM analysis. (**B**) Representative cryo-EM image (scale bar, 50 nm) from 14,740 movies. (**C**) Representative 2D averages (scale bar, 5 nm). (**D**) The focus refinement density map of the binding interfaces between RBDs and Fabs. (**E**) Local resolution for the densities. (**F-G**) 'Gold-standard' FSC curves of the global complex and the RBDs-Fabs interface.

Fig. S6. Structural comparisons of the ACE2-bound and Fab-bound SARS-CoV-2 Omicron Spike protein. (**A-B**) Superpositions of the ACE2-bound and Fab-bound Omicron S trimer. The different protomers are colored. The compared models showed with a front view (A) and a top view (B). (**C**) Superpositions shows ACE2 and the Fab do not share binding sites of S protein RBD.

Fig. 1

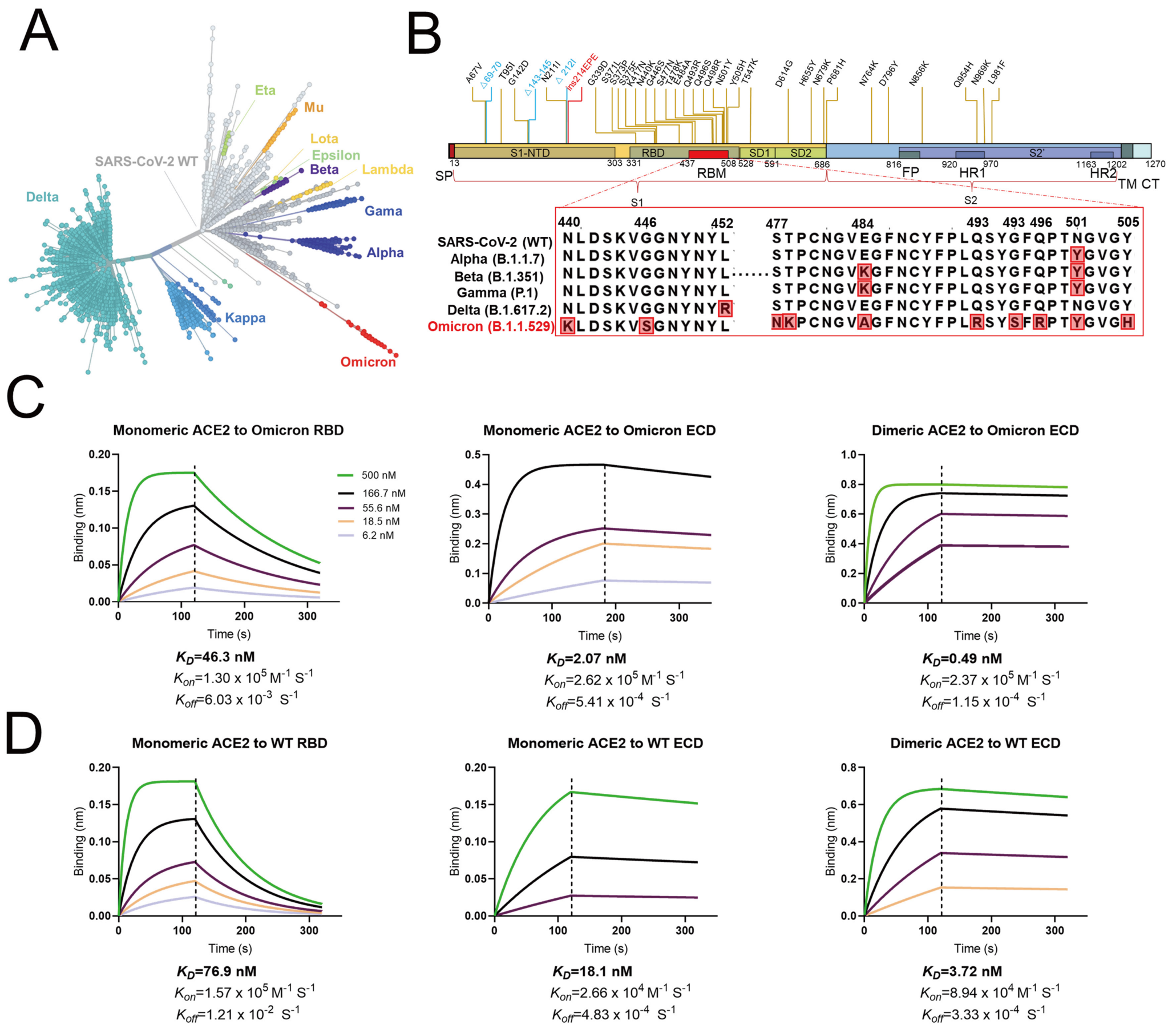
A
Eta
Mu
Lota
Epsilon
Beta
Lambda
SARS-CoV-2 WT
Delta
Gama
Alpha
Kappa
Omicron
B
S1-NTD
RBD
SD1
SD2
S2
SP
RBM
FP
HR1
HR2
TM CT
S1
S2
SARS-CoV-2 (WT)
Alpha (B.1.1.7)
Beta (B.1.351)
Gamma (P.1)
Delta (B.1.617.2)
Omicron (B.1.1.529)
C
Monomeric ACE2 to Omicron RBD
Monomeric ACE2 to Omicron ECD
Dimeric ACE2 to Omicron ECD
Binding (nm)
Time (s)
500 nM
166.7 nM
55.6 nM
18.5 nM
6.2 nM
K_D=46.3 nM
K_{on}=1.30 x 10^5 M^{-1} S^{-1}
K_{off}=6.03 x 10^{-3} S^{-1}
K_D=2.07 nM
K_{on}=2.62 x 10^5 M^{-1} S^{-1}
K_{off}=5.41 x 10^{-4} S^{-1}
K_D=0.49 nM
K_{on}=2.37 x 10^5 M^{-1} S^{-1}
K_{off}=1.15 x 10^{-4} S^{-1}
D
Monomeric ACE2 to WT RBD
Monomeric ACE2 to WT ECD
Dimeric ACE2 to WT ECD
K_D=76.9 nM
K_{on}=1.57 x 10^5 M^{-1} S^{-1}
K_{off}=1.21 x 10^{-2} S^{-1}
K_D=18.1 nM
K_{on}=2.66 x 10^4 M^{-1} S^{-1}
K_{off}=4.83 x 10^{-4} S^{-1}
K_D=3.72 nM
K_{on}=8.94 x 10^4 M^{-1} S^{-1}
K_{off}=3.33 x 10^{-4} S^{-1}

Fig. 2

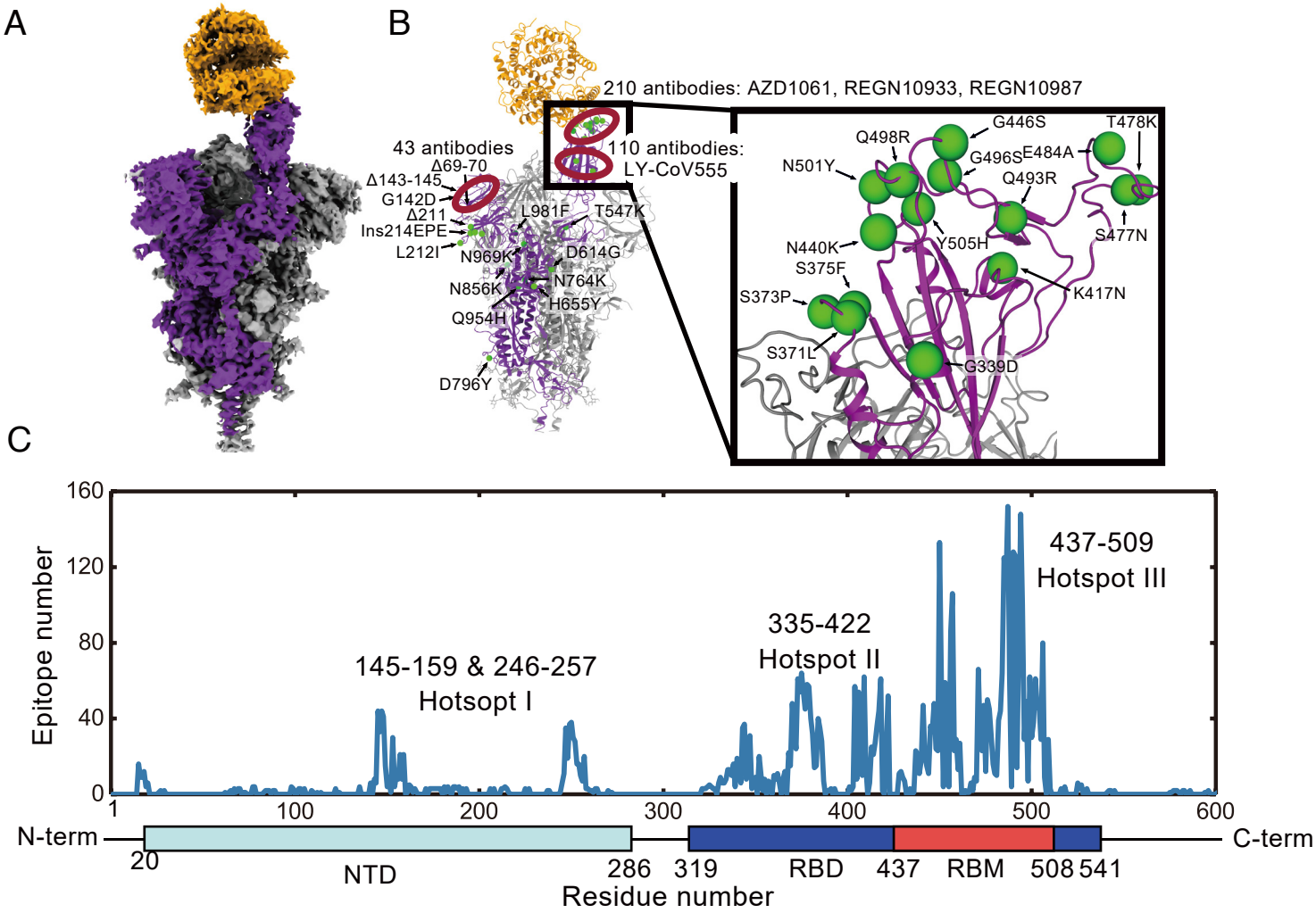
A
B
210 antibodies: AZD1061, REGN10933, REGN10987
43 antibodies
110 antibodies:
LY-CoV555
Δ69-70
Δ143-145
G142D
Δ211
Ins214EPE
L212I
N969K
L981F
T547K
D614G
N764K
N856K
H655Y
Q954H
D796Y
G446S
T478K
Q498R
G496S
E484A
N501Y
Q493R
S477N
N440K
Y505H
S375F
K417N
S373P
S371L
G339D
C
Epitope number
160
120
80
40
0
1
100
200
300
400
500
600
145-159 & 246-257
Hotsopt I
335-422
Hotspot II
437-509
Hotspot III
N-term
C-term
20
NTD
286
319
RBD
437
RBM
508
541
Residue number

Fig. 3

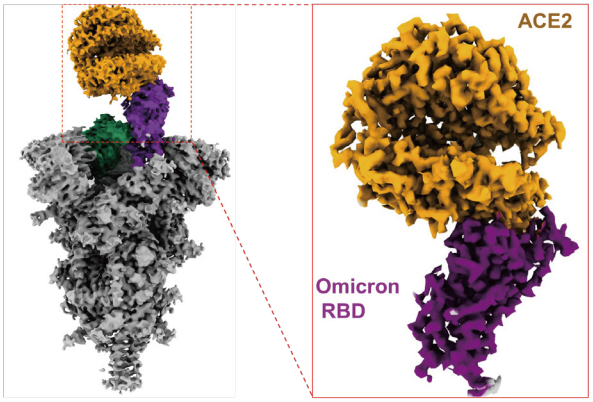
A
ACE2
Omicron
RBD

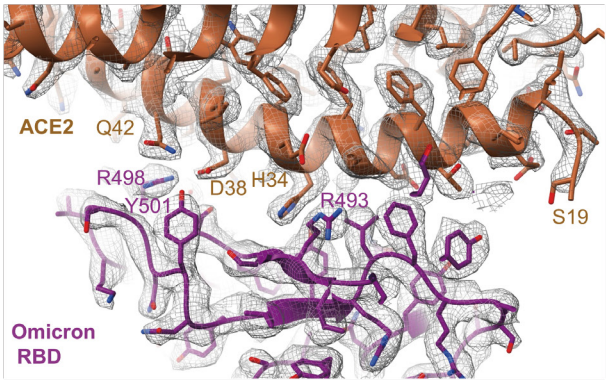
B
ACE2
Q42
R498
Y501
D38
H34
R493
S19
Omicron
RBD

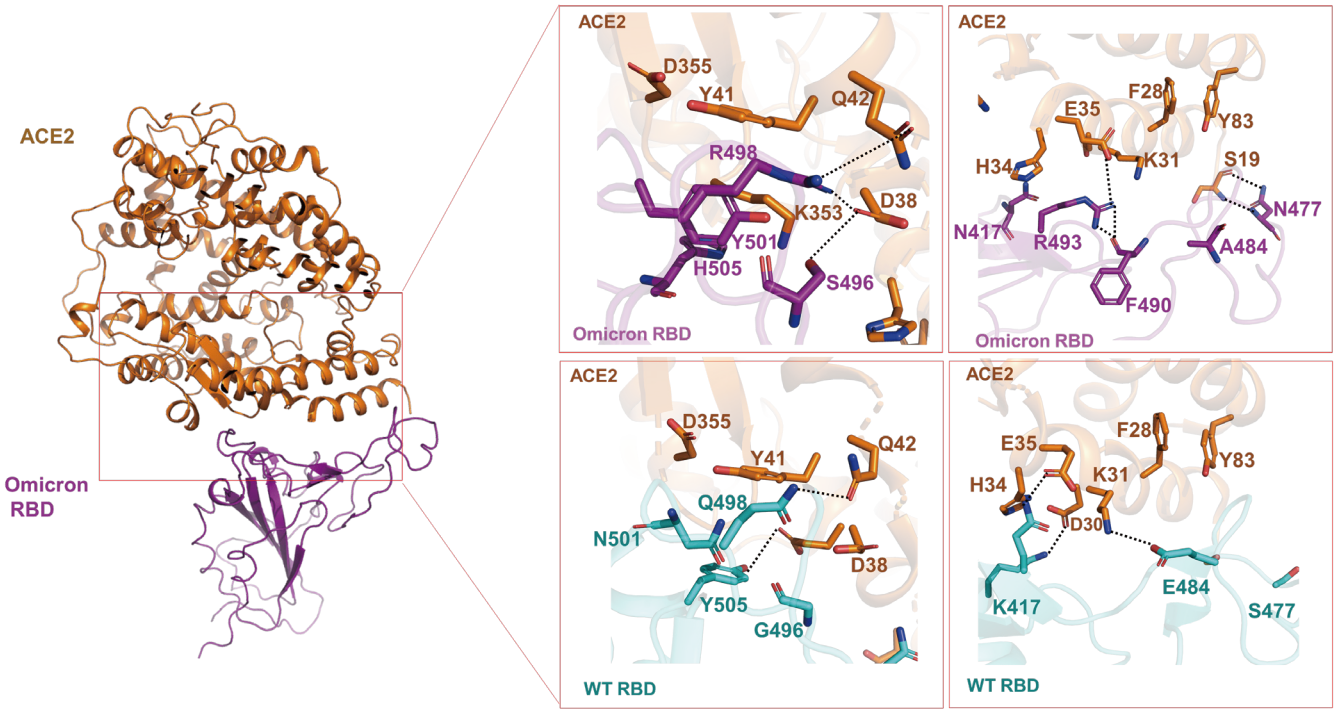
C
ACE2
Omicron
RBD
ACE2
D355
Y41
Q42
R498
K353
D38
Y501
H505
S496
Omicron RBD
ACE2
F28
E35
Y83
H34
K31
S19
N417
R493
N477
A484
F490
Omicron RBD
ACE2
D355
Y41
Q42
Q498
N501
D38
Y505
G496
WT RBD
ACE2
E35
F28
Y83
H34
K31
D30
K417
E484
S477
WT RBD

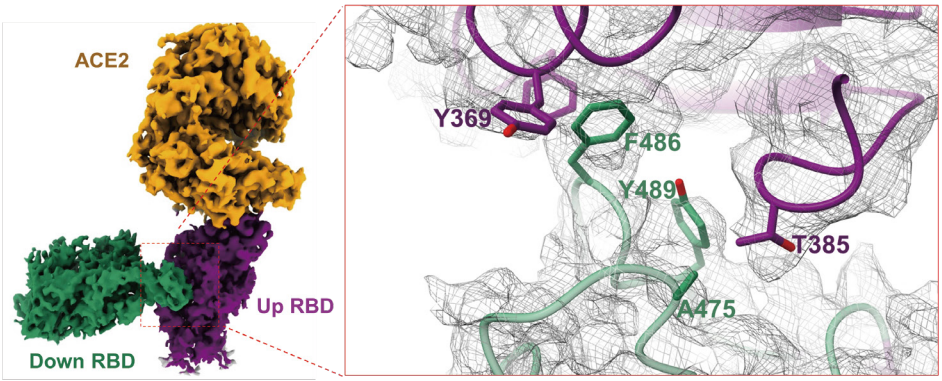
D
ACE2
Up RBD
Down RBD
Y369
F486
Y489
T385
A475

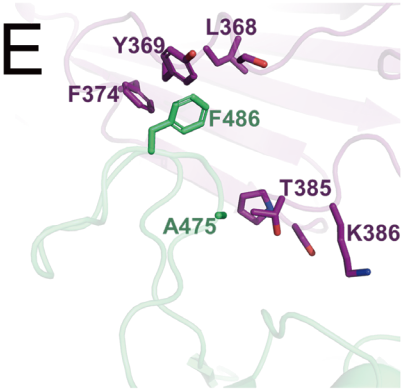
E
Y369
L368
F374
F486
T385
A475
K386

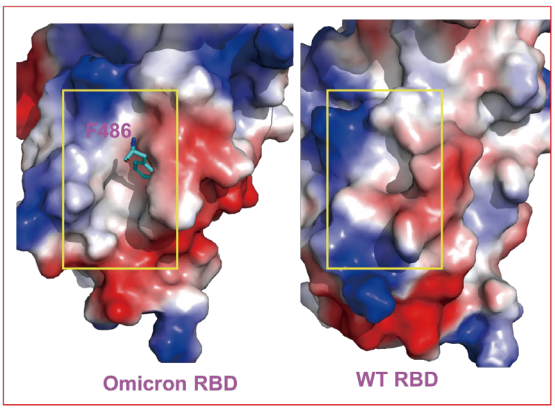
F
F486
Omicron RBD
WT RBD

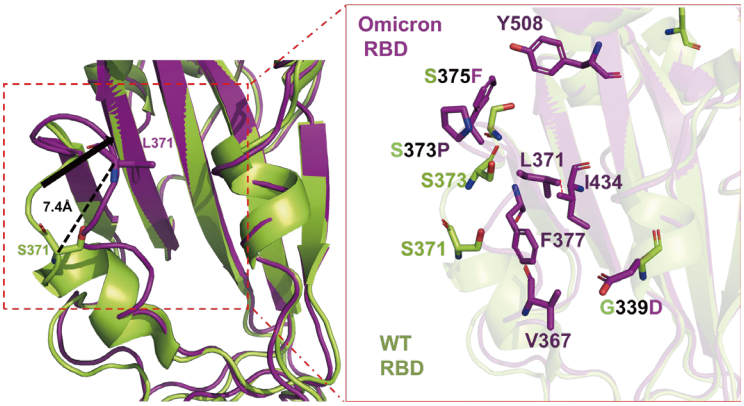
G
L371
7.4A
S371
Omicron
RBD
Y508
S375F
S373P
S373
L371
I434
S371
F377
G339D
V367
WT
RBD

Fig. 4

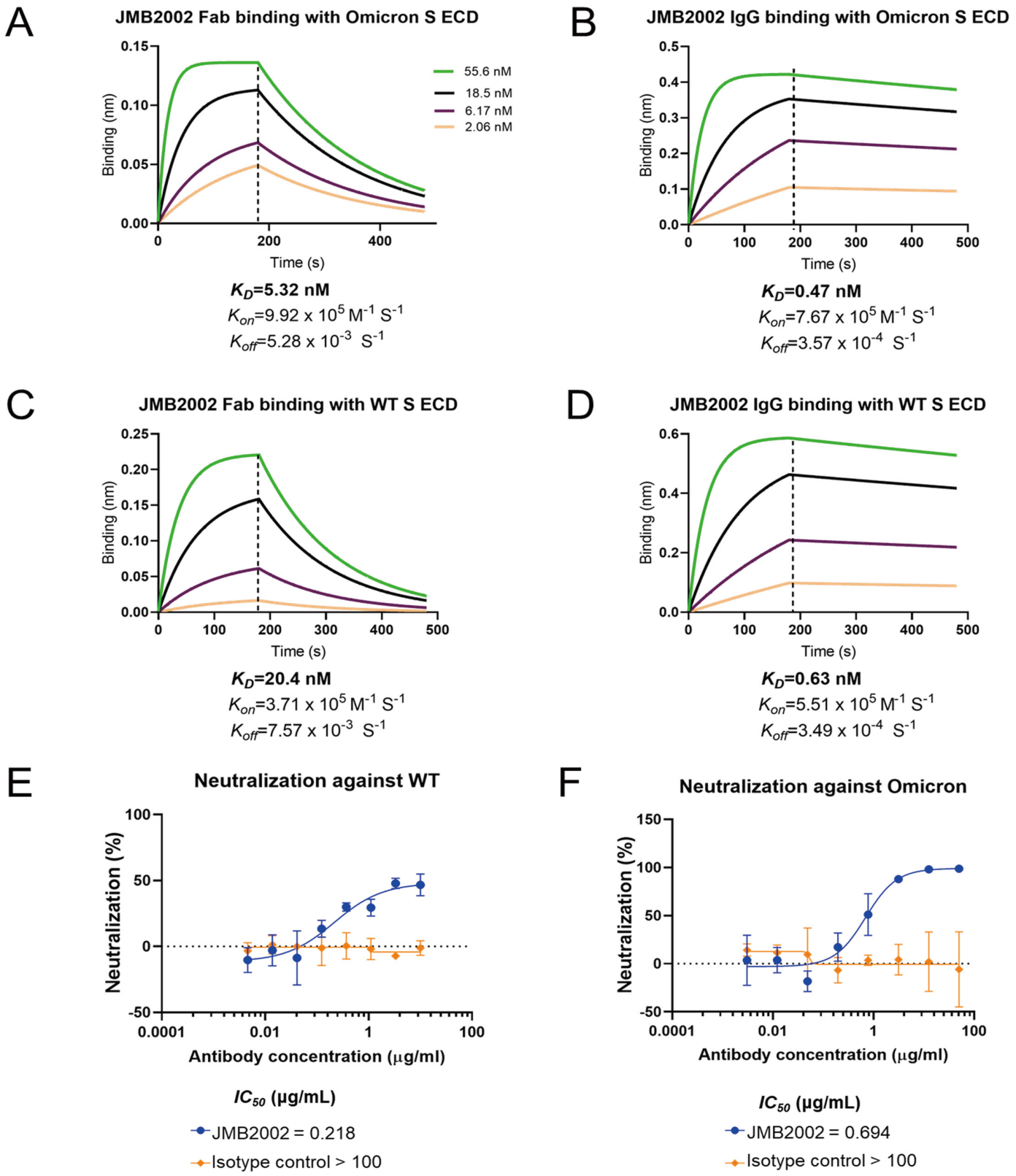
A
JMB2002 Fab binding with Omicron S ECD
Binding (nm)
Time (s)
55.6 nM
18.5 nM
6.17 nM
2.06 nM
K_D=5.32 nM
K_{on}=9.92 x 10^5 M^{-1} S^{-1}
K_{off}=5.28 x 10^{-3} S^{-1}
B
JMB2002 IgG binding with Omicron S ECD
Binding (nm)
Time (s)
K_D=0.47 nM
K_{on}=7.67 x 10^5 M^{-1} S^{-1}
K_{off}=3.57 x 10^{-4} S^{-1}
C
JMB2002 Fab binding with WT S ECD
Binding (nm)
Time (s)
K_D=20.4 nM
K_{on}=3.71 x 10^5 M^{-1} S^{-1}
K_{off}=7.57 x 10^{-3} S^{-1}
D
JMB2002 IgG binding with WT S ECD
Binding (nm)
Time (s)
K_D=0.63 nM
K_{on}=5.51 x 10^5 M^{-1} S^{-1}
K_{off}=3.49 x 10^{-4} S^{-1}
E
Neutralization against WT
Neutralization (%)
Antibody concentration (μg/ml)
IC_{50} (μg/mL)
JMB2002 = 0.218
Isotype control > 100
F
Neutralization against Omicron
Neutralization (%)
Antibody concentration (μg/ml)
IC_{50} (μg/mL)
JMB2002 = 0.694
Isotype control > 100

Fig. 5

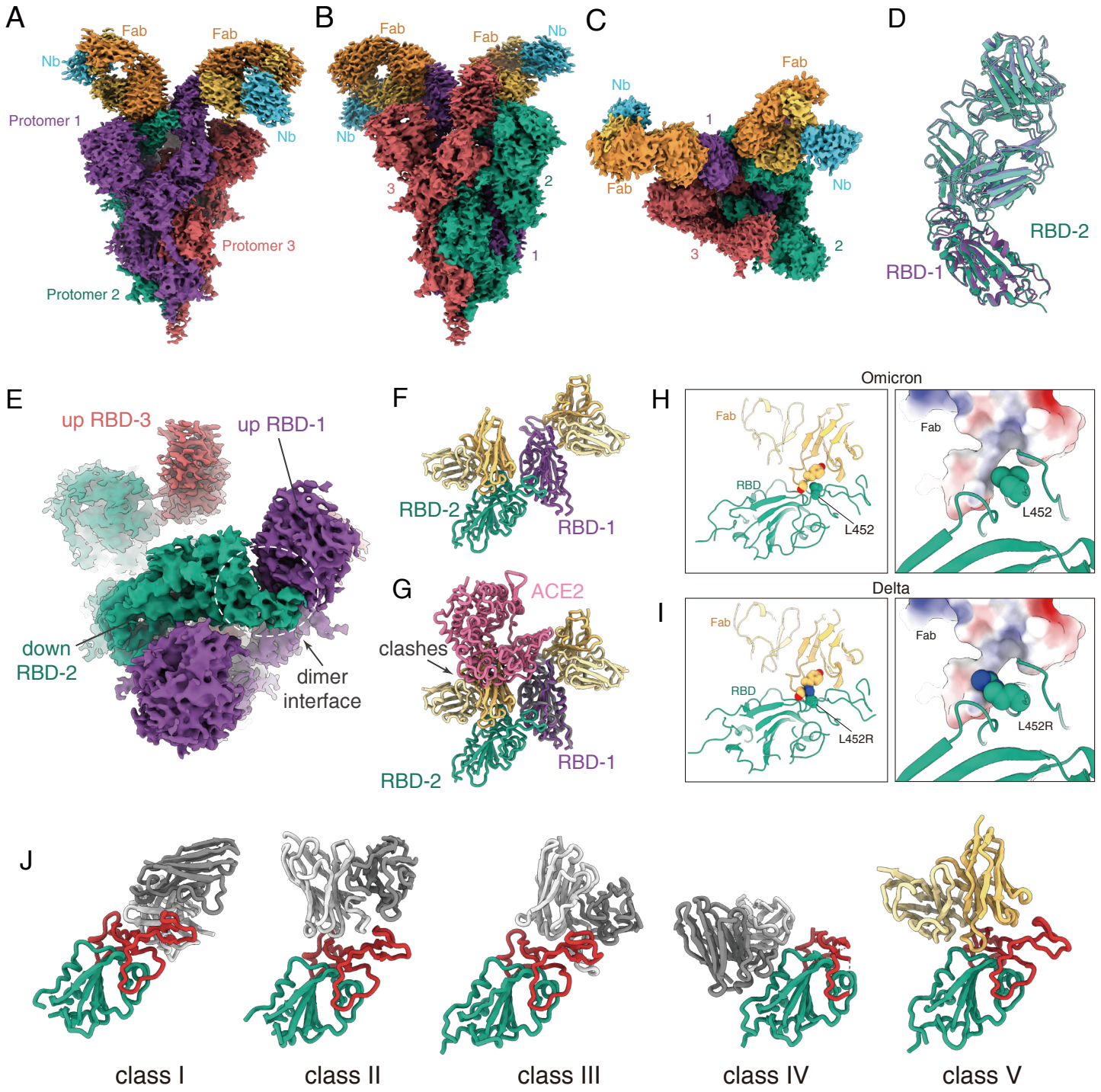
A
Fab
Fab
Nb
Nb
Protomer 1
Protomer 3
Protomer 2
B
Fab
Fab
Nb
Nb
3
2
1
C
Fab
Nb
1
Fab
Nb
3
2
D
RBD-2
RBD-1
E
up RBD-3
up RBD-1
down
RBD-2
dimer
interface
F
RBD-2
RBD-1
G
ACE2
clashes
RBD-2
RBD-1
H
Omicron
Fab
RBD
L452
Fab
L452
I
Delta
Fab
RBD
L452R
Fab
L452R
J
class I
class II
class III
class IV
class V

Table S1 Cryo-EM data collection, refinement and validation statistics

	Omicron ECD-ACE2 complex				Omicron ECD-Fab complex	
Data collection and processing						
Magnification	105,000				105,000	
Voltage (kV)	300				300	
Electron exposure ($e^-/Å^2$)	50				50	
Defocus range (μm)	-0.5 ~ -2.5				-0.5 ~ -2.5	
Pixel size (Å)	0.824				0.824	
Symmetry imposed	C1				C1	
Initial particle projections (no.)	5,071,668				6,563,376	
Sub-maps	Map 1 ECD-Trimer	Map 2 ECD-ACE2	Map 3 RBD-ACE2	Map 4 RBD-ACE2-RBD	Map 1 ECD-2Fab	Map 2 RBD-Fab
Final particle projections (no.)	522,186	242,374	242,374	242,374	421,216	173,847
Map resolution (Å)	2.56	2.77	2.79	2.56	2.76	3.45
FSC threshold	0.143	0.143	0.143	0.143	0.143	0.143
Map resolution range (Å)	2.6-5.5	2.8-6.2	2.8-3.2	2.6-5.5	2.5-5.5	2.5-5.5
Refinement						
Initial model used	6VXX	7A94	7A94	7A94	6VXX	
Model resolution (Å)	3.1	3.9	3.9	3.9	3.0	
FSC threshold	0.143	0.143	0.143	0.143	0.143	
Map sharpening *B* factor ($Å^2$)	-92	-91.3	-107.1	-64.6	DeepEM	
Model composition						
Non-hydrogen atoms			6491	8081	31,989	
Protein residues			793	996	4226	
R.m.s. deviations						
Bond lengths (Å)			0.005	0.007	0.013	
Bond angles (°)			0.873	1.10	1.120	
Validation						
MolProbity score			1.39	0	1.01	
Clashscore			3.63	3.67	0.08	
Rotamer outliers (%)			0.00	0.34	0.11	
Ramachandran plot						
Favored (%)			96.45	94.42	93.05	
Allowed (%)			3.55	5.58	6.95	
Disallowed (%)			0	0	0	

Table S2

A summary of the comparison between our ACE2-RBD^{Omi} structure and selected ACE2-RBD structures.

Our structure Compared with		6M0J	6LZG	6M17	7A94	7KMB	7DF4
Method		X-ray	X-ray	Cryo-EM	Cryo-EM	Cryo-EM	Cryo-EM
Resolution (Å)		2.45	2.5	2.9	3.4	3.39	3.8
RMSD (Å)	Overall	0.49	0.44	0.60	0.87	1.18	1.34
	ACE2	0.49	0.44	0.60	0.83	1.18	1.34
	RBD	0.40	0.34	0.50	0.64	0.66	0.96
Reference (PMID)		32225176	32275855	32132184	32942285	33271067	33277323

Fig. S1

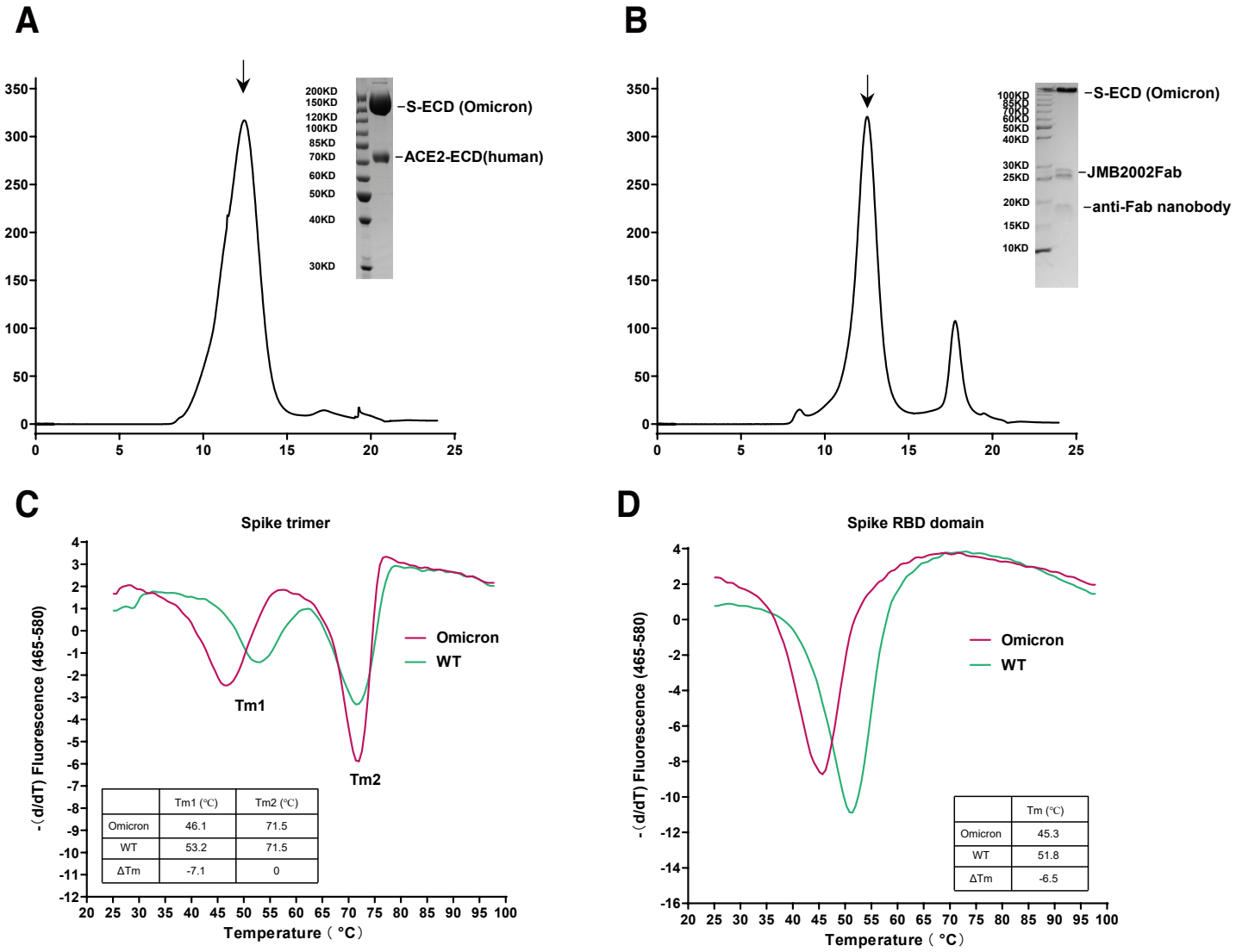

	Tm1 (℃)	Tm2 (℃)
Omicron	46.1	71.5
WT	53.2	71.5
ΔTm	-7.1	0

	Tm (℃)
Omicron	45.3
WT	51.8
ΔTm	-6.5

Fig. S2

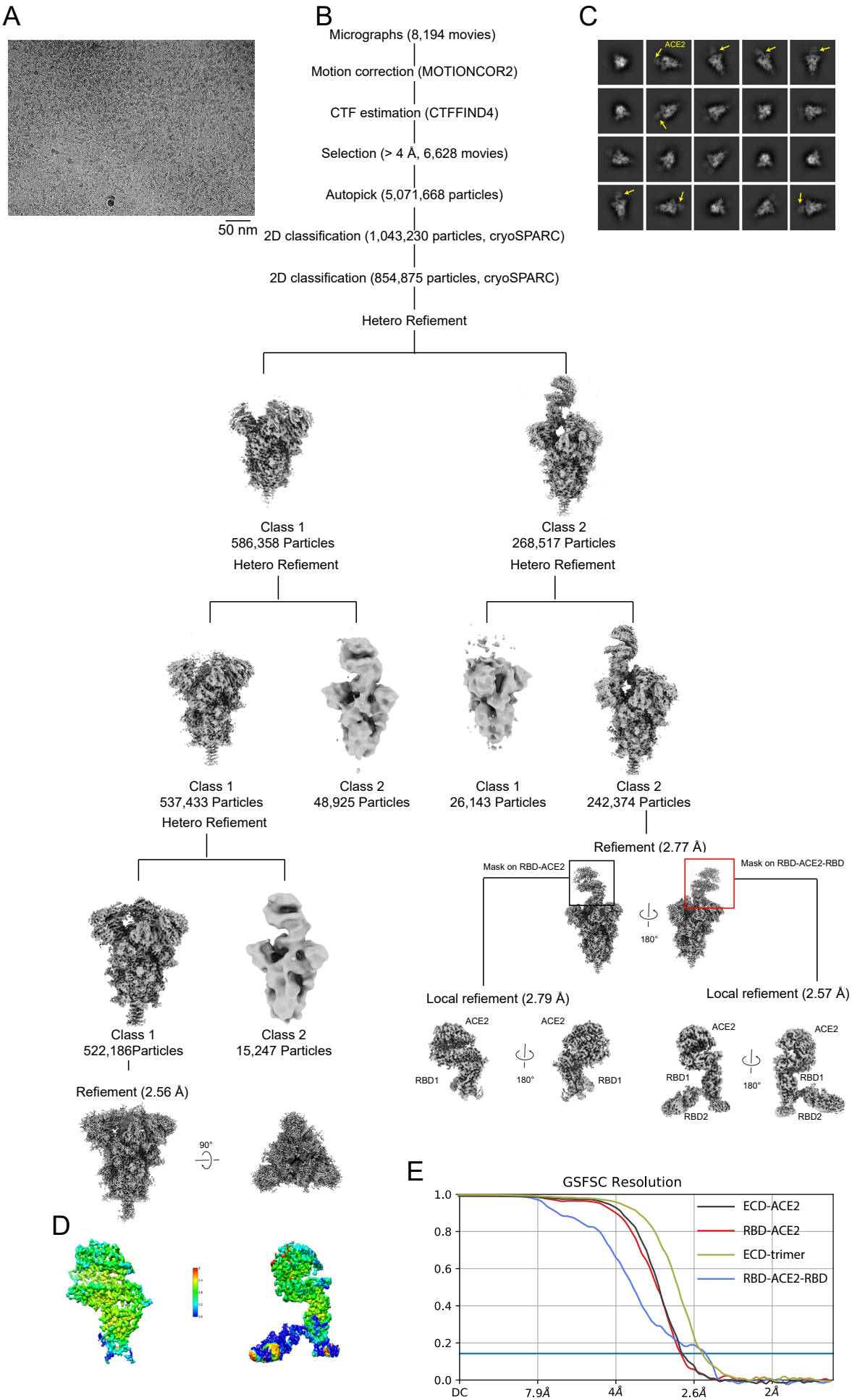
A
50 nm
B
Micrographs (8,194 movies)
Motion correction (MOTIONCOR2)
CTF estimation (CTFFIND4)
Selection (> 4 Å, 6,628 movies)
Autopick (5,071,668 particles)
2D classification (1,043,230 particles, cryoSPARC)
2D classification (854,875 particles, cryoSPARC)
Hetero Refiement
Class 1
586,358 Particles
Hetero Refiement
Class 2
268,517 Particles
Hetero Refiement
Class 1
537,433 Particles
Class 2
48,925 Particles
Class 1
26,143 Particles
Class 2
242,374 Particles
Hetero Refiement
Class 1
522,186Particles
Class 2
15,247 Particles
Refiement (2.56 Å)
90°
Refiement (2.77 Å)
Mask on RBD-ACE2
Mask on RBD-ACE2-RBD
180°
Local refiement (2.79 Å)
Local refiement (2.57 Å)
ACE2
RBD1
RBD2
180°
C
ACE2
D
E
GSFSC Resolution
1.0
0.8
0.6
0.4
0.2
0.0
DC
7.9Å
4Å
2.6Å
2Å
ECD-ACE2
RBD-ACE2
ECD-trimer
RBD-ACE2-RBD

Fig. S3

A

Sharpened high resolution map (2.56 Å, Bfactor=92)

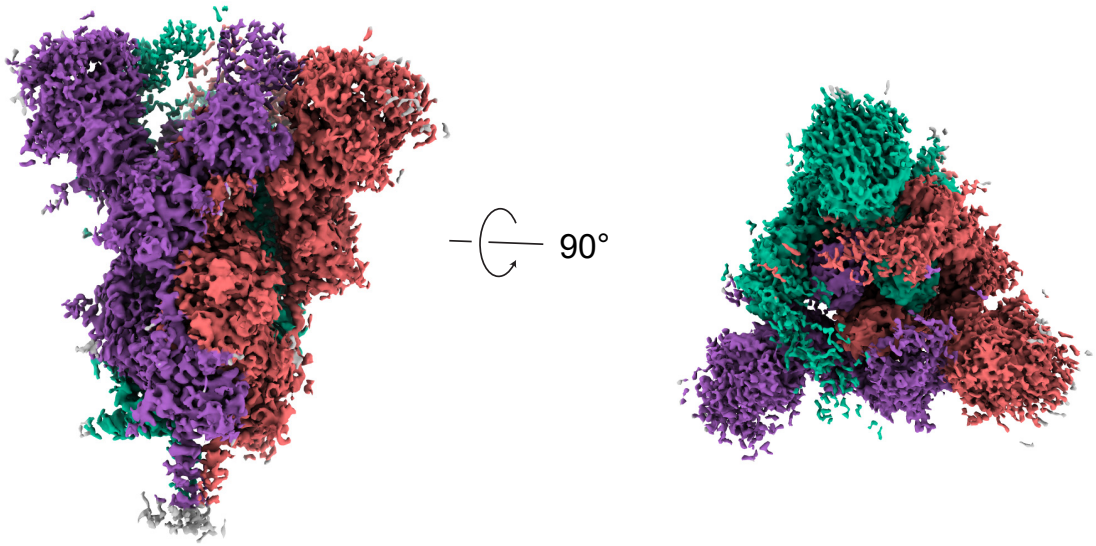

Front view

Top view

B

Unsharpened low resolution map (6.5 Å)

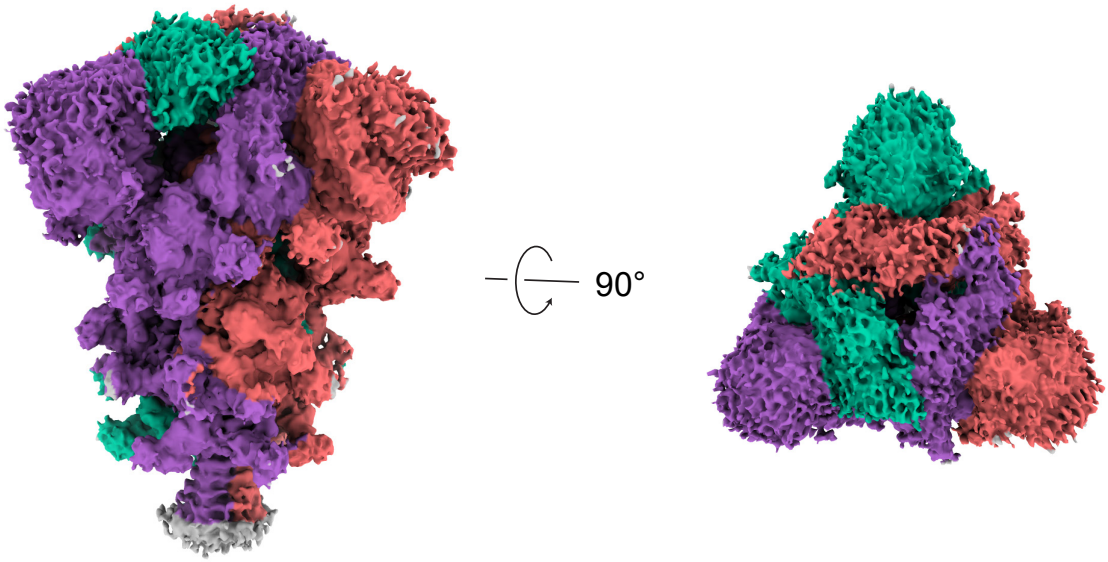

Front view

Top view

Fig. S4

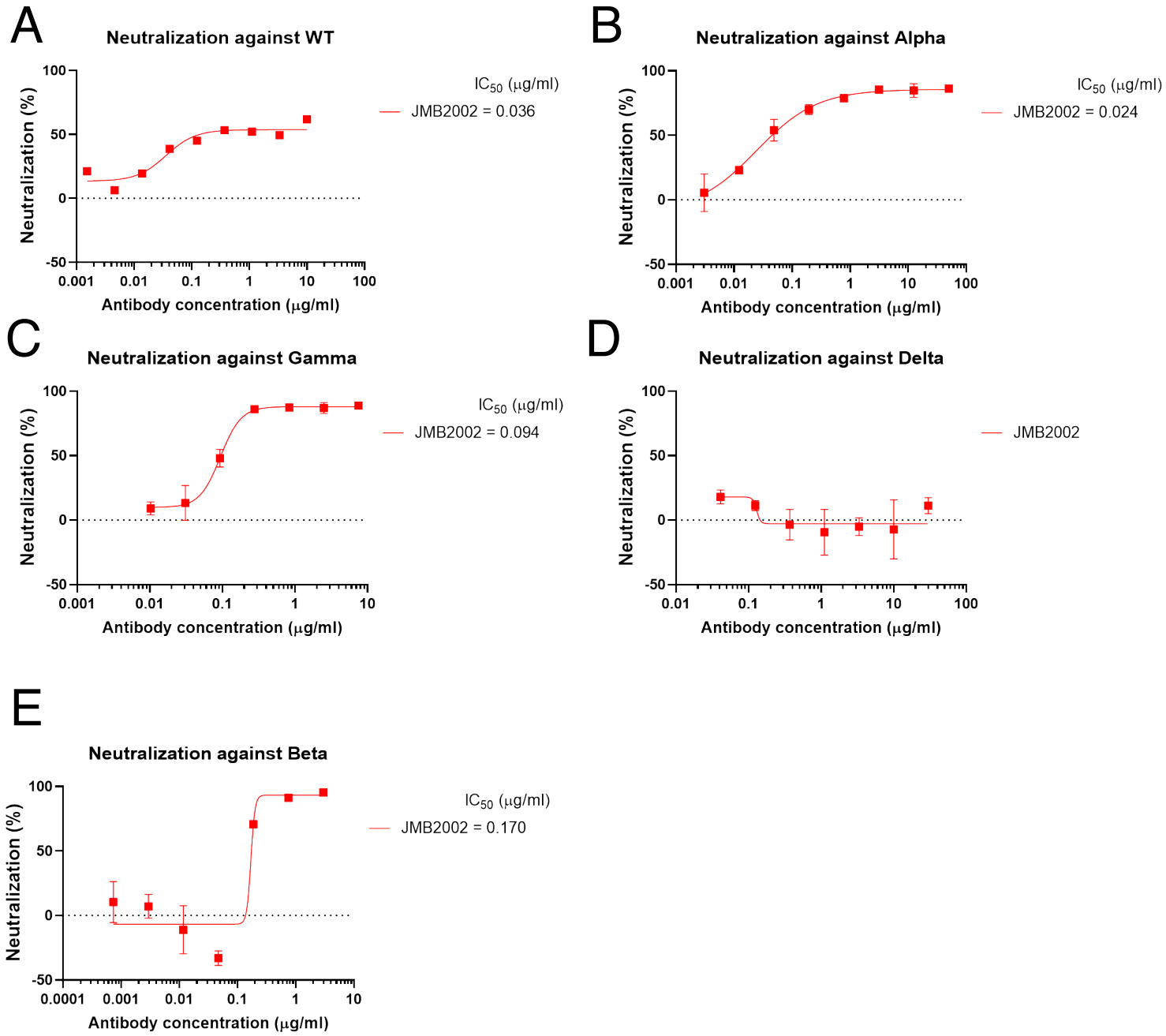
A
Neutralization against WT
Neutralization (%)
Antibody concentration (μg/ml)
IC50 (μg/ml)
JMB2002 = 0.036
B
Neutralization against Alpha
Neutralization (%)
Antibody concentration (μg/ml)
IC50 (μg/ml)
JMB2002 = 0.024
C
Neutralization against Gamma
Neutralization (%)
Antibody concentration (μg/ml)
IC50 (μg/ml)
JMB2002 = 0.094
D
Neutralization against Delta
Neutralization (%)
Antibody concentration (μg/ml)
JMB2002
E
Neutralization against Beta
Neutralization (%)
Antibody concentration (μg/ml)
IC50 (μg/ml)
JMB2002 = 0.170

Fig. S5

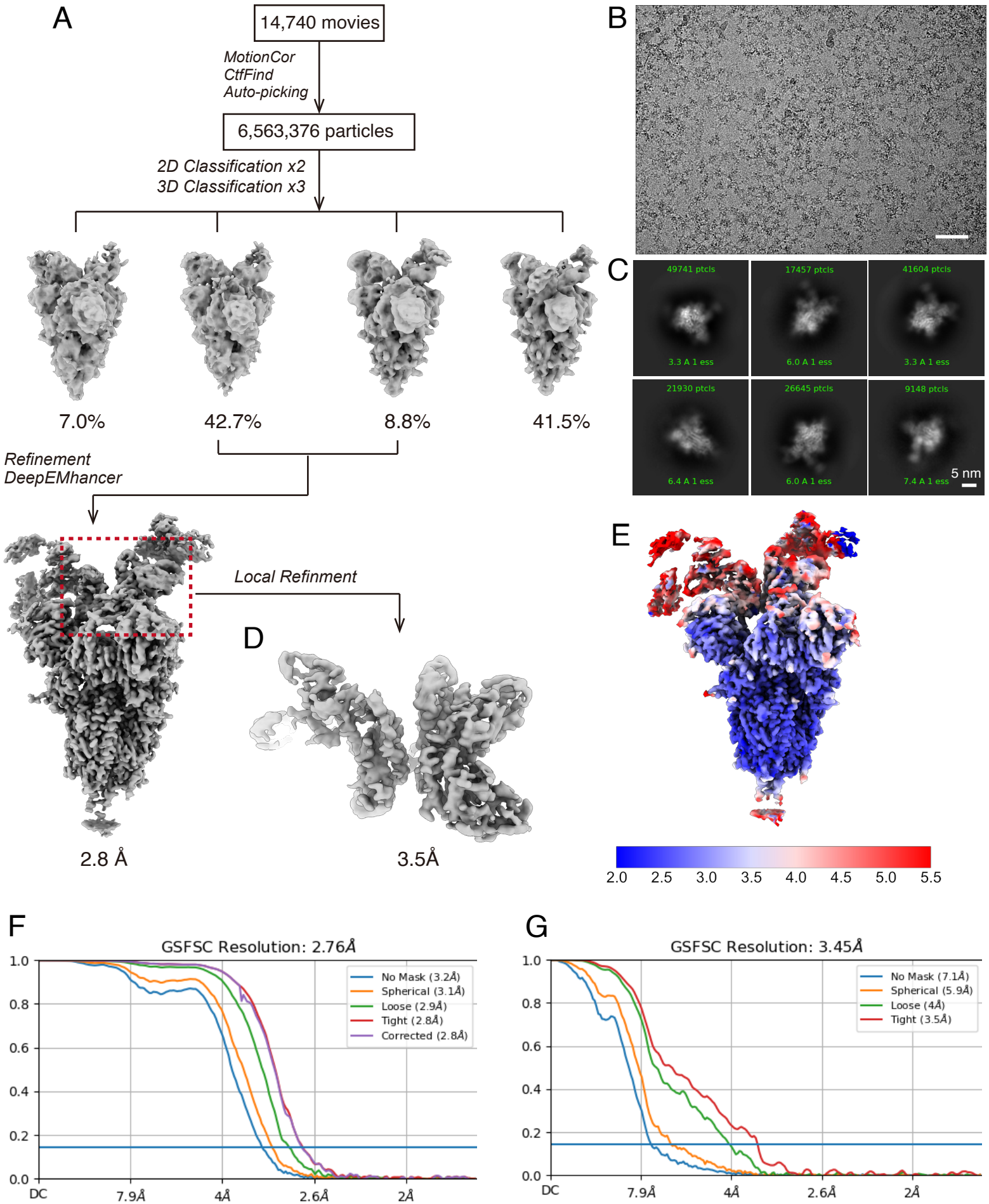
A
14,740 movies
MotionCor
CtfFind
Auto-picking
6,563,376 particles
2D Classification x2
3D Classification x3
7.0%
42.7%
8.8%
41.5%
Refinement
DeepEMhancer
Local Refinment
2.8 Å
D
3.5Å
B
C
49741 ptcls
17457 ptcls
41604 ptcls
21930 ptcls
26645 ptcls
9148 ptcls
5 nm
E
2.0
2.5
3.0
3.5
4.0
4.5
5.0
5.5
F
GSFSC Resolution: 2.76Å
No Mask (3.2Å)
Spherical (3.1Å)
Loose (2.9Å)
Tight (2.8Å)
Corrected (2.8Å)
DC
7.9Å
4Å
2.6Å
2Å
G
GSFSC Resolution: 3.45Å
No Mask (7.1Å)
Spherical (5.9Å)
Loose (4Å)
Tight (3.5Å)

Fig. S6

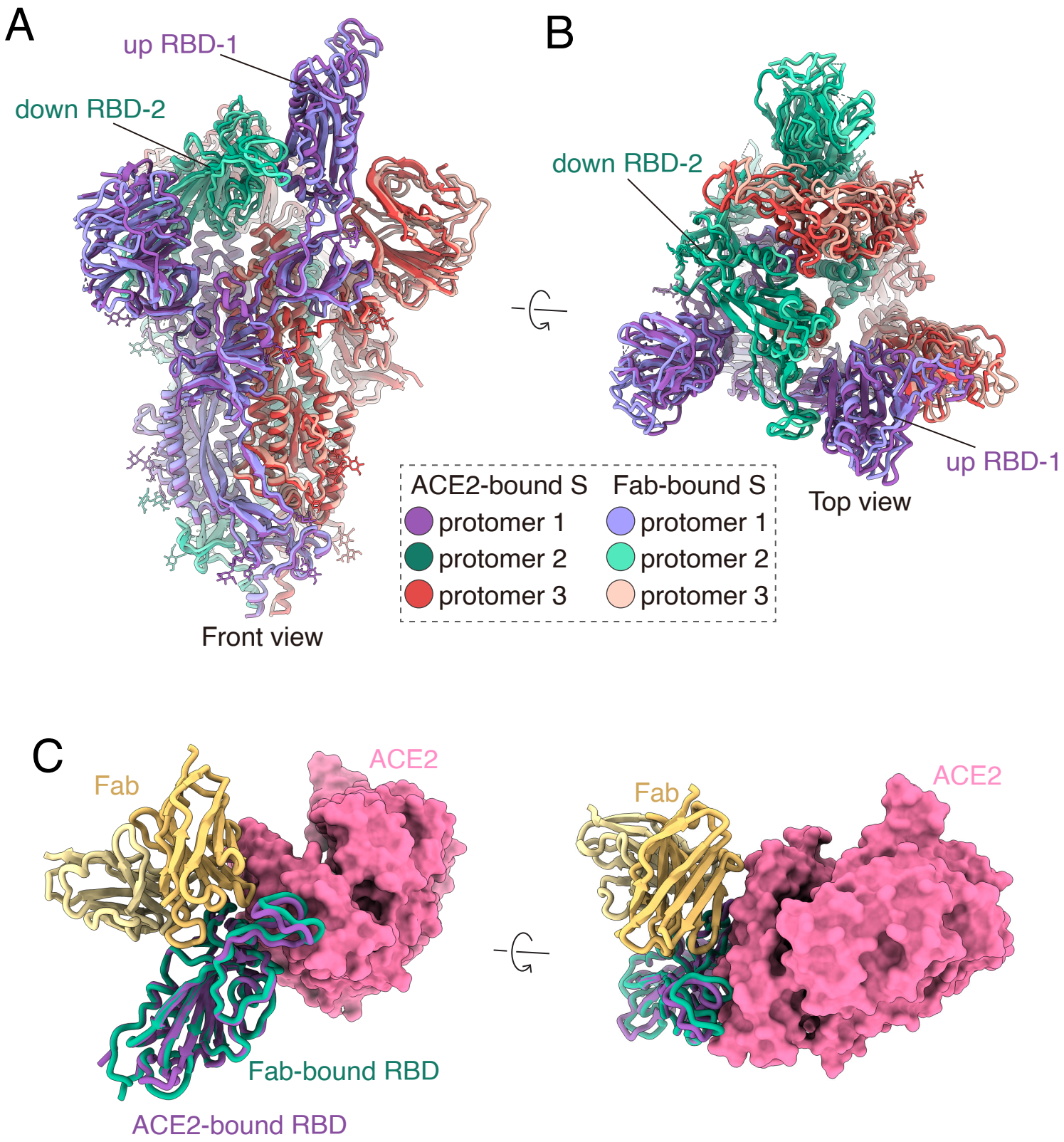
A
up RBD-1
down RBD-2
Front view
B
down RBD-2
up RBD-1
Top view
ACE2-bound S
protomer 1
protomer 2
protomer 3
Fab-bound S
protomer 1
protomer 2
protomer 3
C
Fab
ACE2
Fab-bound RBD
ACE2-bound RBD
Fab
ACE2